

Linking Trehalose Self-Association with Binary Aqueous Solution Equation of State

Liel Sapir and Daniel Harries*

*Institute of Chemistry and The Fritz Haber Research Center, The Hebrew University of Jerusalem, Safra Campus, Jerusalem 91904, Israel**Received: October 12, 2010; Revised Manuscript Received: November 28, 2010*

In aqueous solutions, trehalose possesses a high propensity to form hydrogen bonds with water as well as other trehalose molecules. This hydrogen bonding not only affects water structure but also promotes extensive concentration dependent aggregation of trehalose molecules, which may impact trehalose's role as a protective cosolute to biomacromolecules. To study the association of trehalose in aqueous solutions over a wide concentration range, we used molecular dynamics simulations based on two different force fields, as well as vapor pressure osmometry. By analyzing trehalose cluster size and fractal dimension in simulations, we estimate the cluster percolation threshold at 1.5–2.2 *m*. Experimentally, trehalose solutions showed positive deviations from ideal van't Hoff's law that grew with concentration. These variations in osmotic pressure can be explained using a simple equation of state that accounts for the repulsive excluded volume interactions between trehalose molecules as well as attractions reflected in sugar clustering. We find that simulations with both applied force fields result in reasonable representations of the solution equation of state. However, in contrast to experiments, the balance between the repulsive and attractive trehalose–trehalose interactions in simulations results in a slightly negative deviation from ideality, probably due to the moderately overaggregative nature of the force fields used.

1. Introduction

Illustrious trehalose (α -D-glucopyranosyl- α -D-glucopyranoside, see Figure 1) is a potent bioprotectant used by many organisms in response to harsh environmental stresses, including dehydration and freezing, that diminish available hydration and can seriously damage biomolecules.^{1–3} For example, in response to dehydration, large quantities of trehalose are accumulated by many organisms as they enter a stage of suspended animation termed anhydrobiosis.^{4–7} The biological role of trehalose has been linked to its capacity to maintain the integrity of proteins and biomembranes over long periods of dehydration, thereby enabling macromolecules to return to their regular metabolic state when circumstances become favorable.^{2,4} In this respect, trehalose stands out as a ubiquitous, biologically compatible, protective cosolute (or “osmolyte”) with an impressive ability to stabilize proteins by shifting the folding equilibrium toward the native state.^{8–11} These attributes have also made trehalose an excellent cosolute for biotechnological applications.^{12–16}

The remarkable properties of trehalose have spurred numerous studies, both experimental and computational, aimed at elucidating the molecular basis of its bioprotective propensities (see, e.g., refs 17–19 and references therein). Several molecular hypotheses have been raised to explain trehalose's action, with the most prominent mechanisms involving water replacement,^{4,5,20} water-layering (or water-entrapment),²¹ vitrification,² and water structure/destructuring effects.²² While these mechanisms are not mutually exclusive, and have found support in many experimental and theoretical findings, discrepancies still exist (see refs 23–25 and references therein). Indeed, the mechanism by which trehalose imposes its bioprotective nature is still not fully resolved and may involve several different processes, depending on the particular circumstances.¹⁴

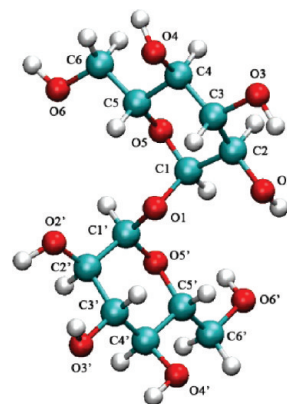


Figure 1. Schematic of trehalose (α -D-glucopyranosyl- α -D-glucopyranoside), with all heavy atoms labeled.

The purpose of this study is to characterize the effect of trehalose on solution structure and, in particular, to follow trehalose self-association in solution. We use molecular dynamics simulations, complemented by vapor pressure osmometry experiments, to describe the concentration-dependent cluster formation of trehalose molecules. We explore two CHARMM-type force fields for carbohydrates that have been developed over the past decade, allowing us to focus on features that are supported by different models, versus ones that may be artifactual or highly force field dependent. By comparing the results from these two force fields with experiment, we have been able to follow the influence of clustering upon solution structure.

Trehalose self-association in aqueous solutions (as well as that of sucrose and maltose) has been extensively studied both computationally and experimentally. The emerging picture, as detailed in the following, indicates that sugar self-associates in aqueous solutions in a concentration dependent manner to form

* To whom correspondence should be addressed. E-mail: daniel@fh.huji.ac.il. Fax: +972-2-6513742.

percolating networks at high concentrations, thereby affecting the solution dynamic properties. Interestingly, it has been argued that the lack of intramolecular hydrogen bonds in trehalose, compared to other disaccharides, accounts for its higher tendency to aggregate,²⁶ thereby making the effect on dynamic properties evident already at lower carbohydrate concentrations.

Carbohydrates are known to have a strong tendency to self-associate in aqueous solutions, leading to concentration-dependent clustering.^{27,28} For example, Molinero et al.²⁹ analyzed computationally the hydrogen bond networks that sucrose forms in aqueous solutions. Their findings were linked to experimental results from other studies of sucrose solutions, and suggested that the formation of sucrose clusters results in the decoupling of water and sucrose diffusion³⁰ and that sucrose percolation is related to the decoupling of viscosity and probe molecule diffusion.³¹ The decoupling of water and sucrose diffusion was further linked with water molecules' trapping inside transient "cages" at high sucrose concentration (~80 wt %).³²

The self-association of trehalose has also gained considerable evidence. Simulations by Lerbret and co-workers^{33–35} showed that trehalose molecules form clusters with sizes that increase with concentration. Eventually, at high enough concentrations of 1.9–2.9 *m*, the sugar hydrogen bond network reaches the percolation threshold. These trehalose hydrogen bond network properties favorably compared with NMR experiments that followed dynamic properties,^{30,32} as described in the following. Concomitantly, the destructuring effect of trehalose on water structure was shown to become more substantial above a concentration of ~1.9 *m*, where it was concluded that the carbohydrate allows only small water clusters to form.³⁶ Similarly to the case of sucrose, simulations of concentrated trehalose solutions at high temperatures also show transient "trapping" of water molecules within "cages" formed by the surrounding trehalose molecules.³⁷ Interestingly, the same restricted diffusion of trehalose molecules within such cages has also been speculated.³⁸

NMR spectroscopy further revealed that the diffusion coefficients of both water and trehalose decrease more rapidly with concentration above ~1.9 *m*. These coefficients more strongly decouple as the concentration increases, with the decoupling becoming more apparent between ~1.9 and 2.9 *m*.³² NMR spectroscopy has not only demonstrated the decoupling between these two coefficients but also showed their decoupling from the solution viscosity at high concentrations.³⁰ This study speculated that the decoupling for supercooled solutions might originate from the formation of an extended hydrogen bond network of sugar molecules. Finally, it has also been suggested that the dependence of trehalose diffusion coefficient on concentration might reflect an aggregative process.^{39,40}

Trehalose self-association has further been demonstrated in ternary mixtures. The simulations of Lins et al. have shown that trehalose at a moderate concentration of 0.5 M can cluster around the protein lysozyme, thereby trapping a thin layer of water molecules with modified solvation properties around the protein.²⁵ Lerbret et al. have followed clustering and percolation of trehalose, sucrose, and maltose in ternary mixtures of lysozyme, sugar, and water, suggesting that the percolation of the sugar's hydrogen bond network increases the relaxation times of all the species in solution and stabilizes the protein by affecting its dynamical properties.^{33,35} More recently, the stability of another protein, CI2, in different polyol and carbohydrate solutions was followed, demonstrating that trehalose and sucrose have a stronger propensity to form clusters than other polyols and sugars.⁴¹ Simulated ternary mixtures of lipid membranes

TABLE 1: Parameters for Simulation Runs

[trehalose] (<i>m</i>)	number of trehalose molecules	number of water molecules
CSFF ⁴⁸		
0.22	15	3841
0.44	30	3824
0.61	36	3292
0.73	45	3445
0.90	54	3338
1.08	60	3086
1.21	72	3307
1.30	75	3200
1.51	75	2765
1.71	90	2924
1.90	90	2626
2.12	90	2357
2.35	105	2477
2.60	105	2242
2.86	105	2039
C35 ^{49,50}		
0.40	30	4117
1.08	60	3081
1.70	90	2933
2.36	105	2472

composed of DPPC (dipalmitoylphosphatidylcholine) in contact with an aqueous solution of trehalose show that trehalose molecules cluster near membrane interfaces, forming hydrogen bonds, both between trehalose molecules and with the lipid headgroups.^{42–44}

In contrast to the variety of solution properties that change significantly at the trehalose cluster percolation threshold, the osmotic pressure of aqueous trehalose solutions at ambient conditions (298 K, 1 bar) follows closely the ideal van't Hoff law in the low concentration regime, while showing only a slight positive deviation from ideality at higher concentrations. This deviation grows with concentration, but to a decreasing extent. Perhaps surprisingly, trehalose solutions, overall, are not far removed from ideal solution behavior.

To resolve this apparent discrepancy, we use a Kirkwood–Buff approach to compare changes in chemical potentials (or solution activities) in both simulations and experiments. We find that simulations provide a reasonable representation of the solution equation of state. This allows us to propose a simple model that can account for the trends in osmotic pressure with concentration, as supported by our computational evidence for trehalose clustering. Our approximate model for the equation of state for trehalose aqueous solutions represents trehalose intermolecular attractions through hydrogen-bonded clusters and accounts for intermolecular repulsions by excluded volume effects. Using this approach, we can dissect the different contributions, both repulsive and attractive, to the trehalose equation of state.

2. Methods and Materials

2.1. Molecular Dynamics (MD) Simulations. All-atom MD simulations of aqueous trehalose solutions over a wide range of concentrations were performed using NAMD.⁴⁵ The water model was TIP3P, and trehalose initial coordinates were taken from the Glycosciences Database (www.glycosciences.de). All interactions were subjected to a CHARMM force field with either of two parameter sets. The first, so-called CSFF, was originally developed by Brady and co-workers^{46,47} and further modified by Kuttel, Brady, and Naidoo.⁴⁸ The second is a CHARMM additive carbohydrate force field developed by MacKerell and co-workers, and termed C35.^{49,50} Table 1 lists

the entire set of simulations performed according to their concentration and the force field used. We note that all simulations of concentrations higher than 2.3 *m* correspond to the supersaturated regime.

All simulations were conducted in the isobaric–isothermic ensemble. Pressure was maintained at 1.01 bar using the Nosé–Hoover Langevin piston method, and the temperature was set to 298 K using the Langevin dynamics algorithm as implemented in NAMD. The simulations were run with periodic boundary conditions within cubic simulation cells with a fluctuating length ranging over all simulations between 46.5 and 51.0 Å. Unless otherwise specified, all bond lengths to hydrogen atoms, as well as the H–O–H angle in water molecules, were kept constant using the SHAKE algorithm. Electrostatic calculations were performed using the Ewald particle-mesh summation with 1 Å grid spacing. Van der Waals interactions were truncated smoothly with a switching distance of 10 Å and a cutoff distance of 12 Å.

Each simulation was started with an energy minimization of 1000 steps and 200 ps of MD equilibration, followed by a production run of 30 ns. We used 2 fs time steps and collected data every 0.5 ps. Only the last 16 ns of each simulation were used for further analysis, giving converged distributions for all simulations. All trajectories were analyzed using VMD.⁵¹ Molecular images were made using VMD⁵¹ and UCSF Chimera.⁵²

As a validation of the simulated binary mixtures, densities of all simulated solutions were compared to interpolation of available experimental data, reported in refs 53 and 54 (see Supporting Information, Figure S1). Simulations with the C35 parameter set gave densities that were in excellent agreement with both sets of experimental data (with deviations of under 1.5% throughout the entire concentration range), as was originally validated by the C35 developers.⁵⁰ Simulations with the CSFF parameter set were also in very close agreement with experimental data, with deviations somewhat increasing with concentration but still lower than 2.5% for the entire concentration range.

Further validation of the simulated solutions was received by comparing the hydrogen–hydrogen pair correlation function $g_{HH}(r)$ from neutron diffraction experiments by Cesaro et al.⁵⁵ with our simulation results (see Supporting Information, Figure S2). For this comparison, we conducted a simulation of 3921 TIP3P water molecules in the absence of trehalose, under the same conditions described for the trehalose solutions. The $g_{HH}(r)$ for pure water and aqueous trehalose solutions, in simulations with both force fields and in experiment, showed good agreement up to a distance of ~ 4.5 Å. Excluding several artifacts caused by the SHAKE algorithm (that fixes the water H–O–H bonds while in reality they fluctuate), the simulation results showed good agreement with experiments. For comparison, several simulations were performed without the SHAKE algorithm and with 1 fs time steps, where all other simulation setup parameters were kept the same: pure water, 1.30 *m* with CSFF and 1.08 *m* with C35. The production run of these simulation was 8 ns long, and only the last 5 ns were analyzed for their $g_{HH}(r)$. The same trend in local density with increasing concentration was seen for both simulation (with and without SHAKE) and experiment for the first two peaks in $g_{HH}(r)$, whereby adding trehalose lowers the first correlation peak and increases the second.

2.2. Vapor Pressure Osmometry. Trehalose dihydrate at a purity of $\geq 99.5\%$ (Fluka) was used as purchased. Samples were weighed with a CP225D weight balance (Sartorius, Goettingen,

Germany) and solvated in water filtered with a Barnstead nanopure Diamond system (Thermo Scientific, Dubuque, IA). Solution osmolalities were measured using a VAPRO 5520 vapor pressure osmometer (Wescor, Logan, UT). All samples were continuously shaken before all measurements. Each data point represents at least three repeats, for which mean values and standard deviations were calculated. The osmometer was initially calibrated using standard NaCl solutions of 290 and 1000 Osm, and recalibrated after ca. every 20 measurements. To assist solvation, the two most concentrated trehalose solutions (2.2 and 2.4 *m*, the second of which is higher than the solubility limit of trehalose) were heated and then allowed to cool to room temperature before measurements were taken. The ambient temperature was set to 298 ± 1 K.

3. Results and Discussion

3.1. Trehalose Impact on Water Structure in Solution.

Trehalose is known to impact the hydrogen bond (H bond) network in aqueous solutions. H bonds were defined in this study as those in which the oxygen–oxygen distance d is less than 3.5 Å and the O···O–H angle θ is less than 30°, as previously suggested.^{56,57} We have verified that this definition, originally suggested for determining H bonding between water molecules, also matches the characteristics of trehalose intermolecular H bonds. Specifically, we find that this definition clearly accounts for the region of high probability density of H bond contacts as a function of d and θ that represent strong H bonding (see Supporting Information, Figure S3).

The distribution of water–water H bonds in trehalose solutions are characterized by a shorter average d in comparison to that found in pure water (3.012 Å for pure water⁵⁸ and 3.006 Å in 1.30 *m* trehalose solution). This difference indicates that trehalose enhances the H bonding within water molecules,^{24,59–61} similar to what was previously shown for other osmolytes both computationally^{58,62} and experimentally.⁵⁹ Using the correlation between H bond length and strength introduced by Espinosa et al., this difference can be semiquantitatively estimated to correspond to $\sim 2\%$ increase in water–water H bond strength (from 24.3 to 24.8 kJ mol^{−1}), a small yet measurable change.⁶³ Moreover, this effect on water–water H bond strength is accompanied by a destructuring of the water tetrahedral network, as was previously shown for trehalose.^{24,34,36,60,64–66} Specifically, one can follow the tetrahedral order parameter, q_i ,^{66,67} defined for the i th water molecule as

$$q_i = 1 - \frac{3}{8} \sum_{j>k} \left(\cos \psi_{ijk} + \frac{1}{3} \right)^2 \quad (1)$$

where ψ_{ijk} is the angle formed between a central water oxygen atom i and two neighboring oxygens j and k (belonging to either water or trehalose). We found that q drops in trehalose aqueous solutions compared with pure water (see Supporting Information, Figure S4), as was also shown for other polyols.⁵⁸ It seems that, in all these solutions, stronger, more linear, and better optimized H bonds are formed between water molecules, while relegating the weaker bonds for trehalose–water interactions. Trehalose–water H bonds follow a similar probability density distribution as a function of d and θ to that of water–water H bonds (data not shown). The simulations show a negligible number of intramolecular trehalose H bonds, as was also previously reported.²⁶

The hydration number of trehalose, defined as the average number of water molecules making H bonds to trehalose, was

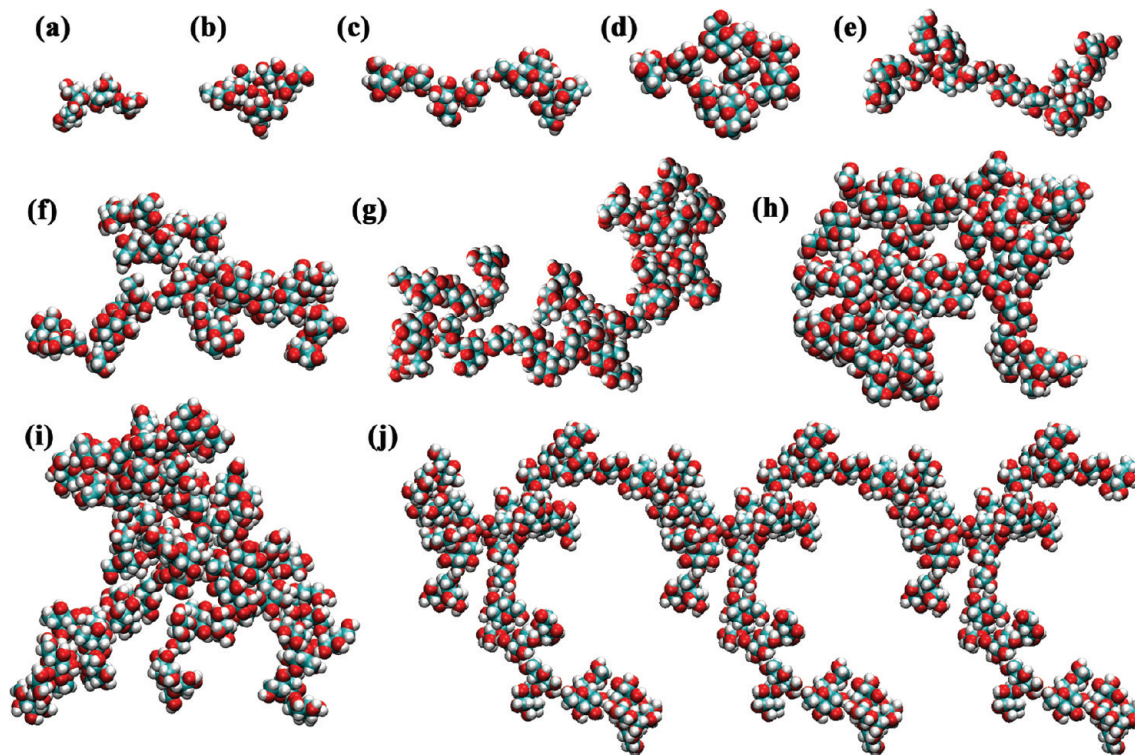


Figure 2. Trehalose molecules bind through H bonds with each other, thereby forming clusters in solution. Shown are typical examples of clusters, as seen in simulations, sorted as aggregates with an increasing number n of molecules (monomers): (a) 2, (b) 3, (c) 4, (d) 5, (e) 8, (f) 15, (g) 22, (h) 30, (i) 37, and (j) an “infinite cluster” that transcends the borders of the periodic simulation cell. All images, shown in VDW representation, are from simulations with CSFF; similar clusters were found using C35.

~ 15 for both CSFF and C35 when extrapolated to infinite dilution. With both force fields, the hydration number decreases by about one water molecule per molal. While estimates of hydration numbers vary between studies and criteria used, the numbers we find are in very good agreement with computational and experimental values previously published for low concentrations^{34,37,54,68} (though some studies reported different values in the range 6–28, see ref 34 and references therein). We return to discuss water ordering around trehalose in section 3.5.

3.2. Trehalose Molecules Form Clusters in Aqueous Solution. To discuss trehalose self-association, we define clusters as an assembly of trehalose molecules that share at least one H bond with another trehalose molecule in the cluster. This criterion ensures that neighboring trehalose molecules in a cluster are associated with at least the strength of one H bond. As we show in the following sections, this criterion also corresponds to strong pair correlations between neighboring trehalose molecules. Representative examples of clusters formed in the simulation are shown in Figure 2, where each identified trehalose cluster was characterized according to its size, defined as the number of molecules composing it, n . A wide distribution of sizes was identified for each of the simulated concentrations.

Figure 3a shows the variation with concentration of the fraction of trehalose molecules present in clusters of size n , $X_n = N_n / \sum_n N_n$, where N_n is the total number of molecules in clusters of size n . The value of X_n for all finite clusters, excluding both monomers and “infinite” clusters that span the entire simulation box beyond the periodic boundaries (see further discussion below), were grouped together, $X_{fin} = \sum_{n=1,\infty} X_n$. Figure 3a clearly shows that, as concentration grows, more trehalose molecules are found residing in clusters (in green) while the number of monomers (in black) decreases. For concentrations above ~ 1.75 m, the fraction of molecules in finite

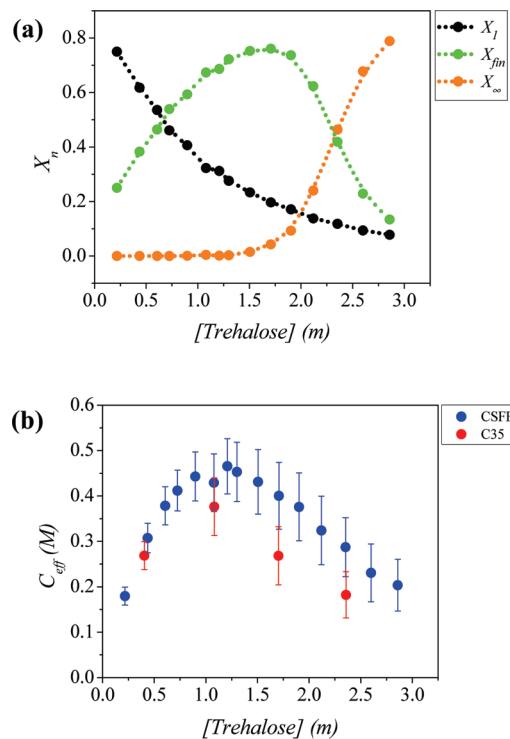


Figure 3. Trehalose clusters grow with concentration. (a) Fraction of trehalose molecules present in clusters of various sizes X_n versus trehalose concentration. Data represent simulations run with the CSFF parameter set (the C35 parameter set gave similar results). (b) Effective solute concentration (average number of clusters or monomers per simulated volume) in simulations versus actual trehalose concentration.

clusters decreases due to the growing dominance of infinite clusters (in orange).

Another manifestation of trehalose clustering is the reduction in the effective number of solvated particles (trehalose clusters and monomers) in solution, N_{eff} . Each of the simulated concentrations displayed an N_{eff} distribution centered around a well-defined maximum at the average $\langle N_{\text{eff}} \rangle$. This number of particles allowed us to calculate the effective particle concentration $C_{\text{eff}} = \langle N_{\text{eff}} \rangle / N_{\text{AV}} V$ for each simulation, where N_{AV} is Avogadro's number and V is the volume. Figure 3b shows the dependence of C_{eff} on the actual concentration of trehalose (given on the molal scale). While at low concentrations C_{eff} grows linearly with molality, for higher concentrations (beyond ~ 1.0 m) clusters become more prevalent, and more molecules participate in infinite clusters. For those higher concentrations, the addition of trehalose molecules only decreases the effective number of particles in the solution, hence lowering C_{eff} .

The temporal autocorrelation functions of cluster size, averaged over all molecules, demonstrated that the simulated systems were well equilibrated and that clustering did not result in kinetic traps. The curves for these functions could be well fit by a double exponential decay (data not shown). The two emerging typical time scales averaged over the entire concentration range are 11 and 360 ps. These time scales may be roughly attributed to clusters changing in size by losing monomers (shorter time scale) and breaking of clusters to fragments (longer time scale). This suggests that clusters are short-lived, with the longer decay time still under 0.5 ns, and that the presence of each monomer molecule in a cluster is short compared to the overall analyzed times for each simulation trajectory (16 ns). We stress that these estimated times only serve to validate the applicability of our results, and that these dynamic properties need not reflect actual experimental values. Indeed, it has been shown that the C35 force field can yield misleading dynamic properties (such as diffusion constants) for concentrated trehalose solutions, even when scaling by the ratio of model water and real water viscosities is applied.⁶⁹ Additional confirmation of the attainment of equilibrium in each of the simulations was gained through comparisons of radial pair correlation functions derived using different time segments along each trajectory (data not shown). These comparisons clearly showed that these distributions were independent of time.

3.3. Trehalose Clusters Reach the Percolation Threshold at Approximately 1.5–2.2 m. Some clusters were occasionally found to span the entire length of the simulation box and were linked through at least one H bond to a molecule on the other side of the periodic simulation box. For the purposes of this study, these clusters were considered “infinite” in the sense that they represent percolating clusters. To analyze these clusters, the entire set of molecules composing each infinite cluster was duplicated, translated, and copied at box width distances along one or more axes where the transcending H bond was formed. Figure 2j shows one such percolating cluster, which was infinite across a single axis of the simulation box. All the structural analyses of percolation clusters were performed on similarly replicated structures.

Figure 4 shows the fraction of trehalose molecules associated with percolation clusters (X_{∞}) as a function of concentration. Both CSFF and C35 force fields show a steep rise in X_{∞} beyond a certain threshold concentration. Such an increase in X_{∞} is characteristic of systems undergoing percolation. For infinite (macroscopic) three-dimensional systems that can undergo percolation, the value of X_{∞} is zero below the percolation threshold, whereas at the threshold the clusters follow a geometrical phase transition.^{70,71} However, in our simulations, finite size effects smoothed the variation of X_{∞} with concentra-

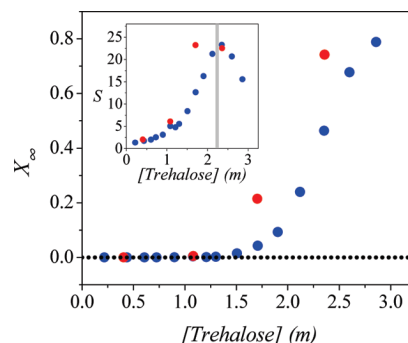


Figure 4. The fraction of trehalose molecules present in percolation clusters increases sharply at the percolation threshold. Shown is X_{∞} versus trehalose concentration for the CSFF and C35 parameter sets. Inset: Mean cluster size of all finite clusters, S , as a function of concentration for both force fields. The gray bar represents the approximate concentration region, where S reaches a maximum for CSFF. Color scheme for both force fields is as in Figure 3b.

tion and, in addition, may have somewhat shifted the value of the percolation threshold concentration, as expected for finite sized systems.^{70,72}

The inset of Figure 4 shows the change with concentration in the mean cluster size of all finite clusters and monomers, S , defined as

$$S = \frac{1}{1 - X_{\infty}} \sum_{n \neq \infty} n X_n \quad (2)$$

For a macroscopic system, S is known to diverge around the percolation threshold.^{70,71} However, because of finite size effects, only an apparent maximum in S is seen in our simulations (Figure 4, inset), which can be identified with the percolation threshold. We used this criterion to estimate the threshold for both parameter sets, finding the apparent percolation threshold obtained with the CSFF parameter set to be ~ 2.2 m, while for C35 we find a lower concentration threshold of ~ 1.5 – 2.0 m. With this measure, we can conclude that the C35 trehalose molecules are somewhat more prone to self-association. It is worth emphasizing that as with all other parameters we had followed, the percolation threshold was also found to be time independent in the simulation.

Our estimate of the percolation threshold is close to that found using a somewhat different criterion for percolation by Lerbret and co-workers (1.9 – 2.9 m).^{33–35} This 1.5 – 2.2 m range, at which we identify the percolation threshold, is very close to but lower than the experimental solubility limit of the sugar: 2.3 m at $T = 298$ K.⁷³ This proximity suggests that the percolation clusters could represent initial stages of precipitation of excess trehalose molecules. This is analogous to previous suggestions that the glass transition temperature of highly concentrated aqueous trehalose solutions (above 80 wt %) can be related to the percolation threshold of water molecules.⁷³ Notwithstanding, it is known that in different solutions and mixtures the percolation threshold need not coincide with the thermodynamic phase transition, and that, depending on system properties, percolation could be reached at lower or higher concentrations than the thermodynamic transition.^{74,75}

3.4. Cluster Fractal Dimension Grows with Trehalose Concentration. To gain further insight into the solution percolation properties, we followed changes in the fractal dimension of clusters. The average mass fractal dimension, \mathcal{D} , of trehalose clusters at each concentration was derived using

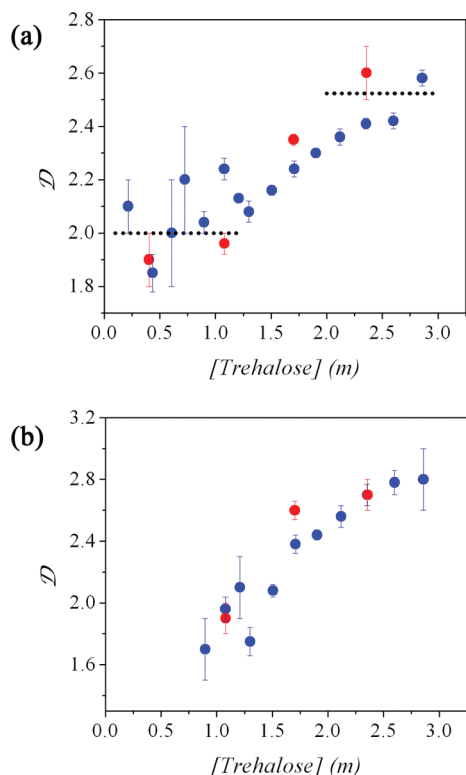


Figure 5. The fractal dimension, \mathcal{D} , increases with concentration for (a) finite clusters and (b) percolation clusters. Dotted lines in plot (a) represent the values of \mathcal{D} for randomly branched polymers with short-range repulsions or linear chains with no interactions ($\mathcal{D} = 2.0$, for the low concentration range) and the value of \mathcal{D} for percolation clusters (2.524, higher concentration range). Error bars represent standard deviations derived using a bootstrapping method. Color scheme for both force fields is as in Figure 3b.

the general scaling relation $n \sim R_g^{\mathcal{D}}$ that relates the number of molecules in a cluster, n , to the cluster's radius of gyration, R_g .^{71,76} For each cluster, we recorded R_g for all constituent molecules present in a concentric sphere of radius r around its center of mass. The value of \mathcal{D} was then determined from the slope of a linear fit to plots of $\ln n$ versus $\ln R_g$. For each simulation, the fractal dimension was derived separately for finite and infinite (percolating) clusters.

Figure 5 shows the dependence of \mathcal{D} on trehalose concentration for finite (Figure 5a) and percolation (Figure 5b) clusters. For finite clusters, the fractal dimension undergoes an evident shift between two regimes around the percolation threshold, probably due to a change in the pattern of cluster growth. For these clusters, \mathcal{D} increases from ~ 2.0 for concentrations under $1.25 m$ to ~ 2.5 above $2.0 m$ (Figure 5a). The value of \mathcal{D} at the lower concentration region is consistent with the value known for randomly branched polymers with short-range repulsions, or linear chains with no interactions.⁷⁶ However, the coordination number distribution for trehalose molecules, discussed below, shows that, for this regime, linear growth is probably the more applicable mechanism. In contrast, for higher concentrations, finite clusters approach the known value of $\mathcal{D} = 2.524$ for infinite clusters around the percolation threshold.⁷⁰ We suggest, therefore, that these large finite clusters may be on the verge of percolation.

For percolating clusters, \mathcal{D} increases with concentration (Figure 5b); however, below the percolation threshold only few infinite clusters were identified. This resulted in poor statistics that did not allow an accurate assessment of \mathcal{D} under $\sim 1.5 m$ (Figure 5b). The calculated \mathcal{D} around the percolation threshold

is close to 2.5, which is also in excellent agreement with the known value of \mathcal{D} for percolation clusters at this threshold.⁷⁰ As expected, \mathcal{D} continues to grow above the percolation threshold, as the clusters gradually become more compact.

3.5. Spatial Organization of Trehalose Self-Association Shows Two Preferred Interaction Regions. To probe the spatial distribution of associated trehalose molecules, we followed the trehalose–trehalose pair correlation function, as well as the corresponding spatial density distribution of the subset of directly H bonded trehalose molecules. Due to its relative rigidity over time, the C1–O1–C1' plane (see Figure 1) was used as the reference coordinate system, as previously employed for water distribution around trehalose in a binary mixture.⁷⁷ The vector connecting the O1 atoms of each pair of trehalose molecules was used as a measure of the intermolecular distance.

Figure 6a,b depicts regions of high density in the pair correlation function (over 1.24-fold the bulk solution density, lobes in red) as well as regions of high probability density for finding directly H bonded trehalose molecules (in blue) around a given molecule. Two regions overlap for both distributions, showing preferential proximity between neighboring molecules. This overlay indicates that the two distributions correlate well, validating our assertion that H bonds mediate the self-association of trehalose and can be faithfully used to define trehalose clustering in solution. The two-lobe pattern, seen in Figure 6 for the $1.30 m$ simulation using CSFF, persisted over the entire concentration range we have tested, as well as in simulations using C35 (see Supporting Information, Figures S5 and S6, respectively).

A certain smearing of the two lobes in Figure 6a,b is caused by conformational fluctuations in the central molecule that serves as a reference frame. However, these fluctuations are quite small, so that the spatial distribution clearly shows that neighboring trehalose molecules preferentially localize close to the central molecule's many hydroxyl groups. This proximity results in intermolecular trehalose–trehalose H bonds, evidenced in the blue isosurfaces in Figure 6a,b. Figure 6c,d shows several examples of trehalose pairs that occupy the two lobes seen in Figure 6a,b. The relative orientations of these pairs demonstrate that trehalose preferentially interacts with neighboring sugar molecules through intermolecular H bonds.

Figure 7 shows the water molecules' spatial distribution around trehalose, which is in good agreement with the findings by Liu et al.⁷⁷ These water molecules are arranged in a solvation shell around trehalose, with the main correlation peaks close both to the central trehalose molecule, and to the trehalose–trehalose correlation peaks. While this pattern of water density around trehalose probably mainly reflects water association with the trehalose functional groups through H bond formation, the presence of water molecules at these sites could also assist in the self-association of trehalose molecules through bridging water molecules.

The spatial distributions in Figure 6a,b can be related to the fractal dimension by following the trehalose coordination number, N_c , defined here as the number of directly H bonded trehalose molecules to any other trehalose molecule. Figure 8 shows the probability distribution of the coordination number of trehalose molecules for several concentrations. As expected, the average coordination number becomes larger as the concentration increases. Moreover, as the probability of finding monomers decreases (Figure 3a), there is a growing probability for finding trehalose molecules with $N_c > 2$. Interestingly, however, the most probable coordination number remains lower than 3 for all concentrations examined.

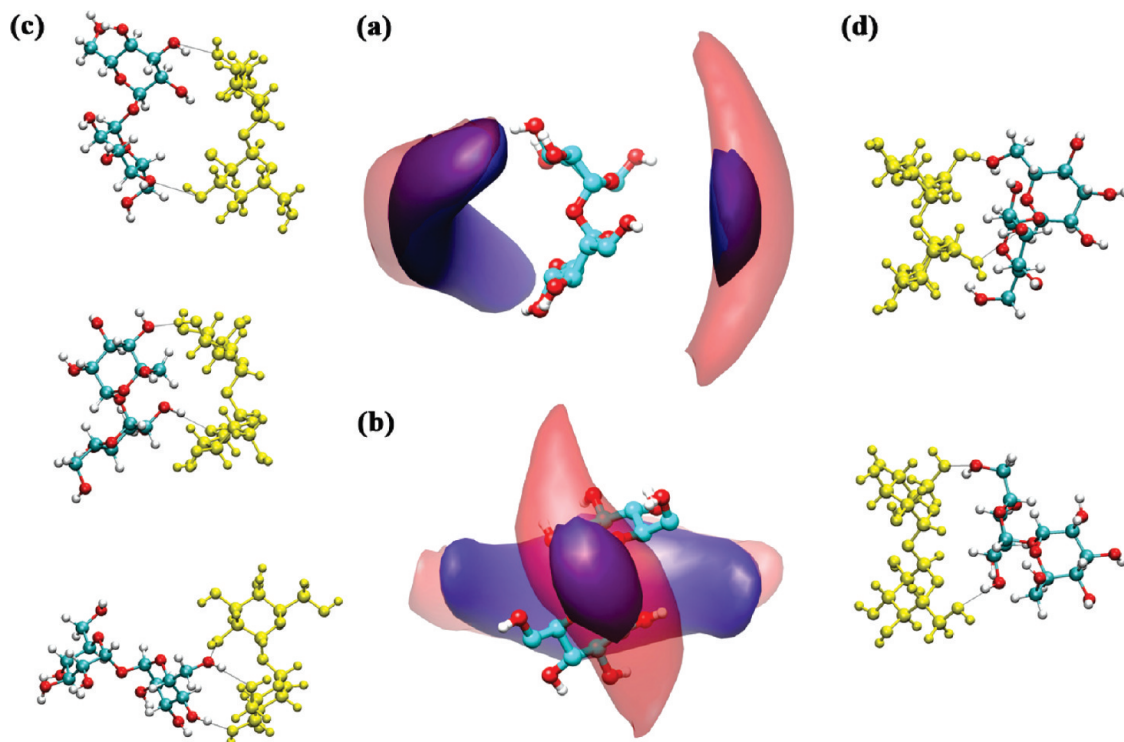


Figure 6. Trehalose self-interaction occurs primarily at two extended regions that also allow H bonding. (a, b) Two projections of spatial density distribution of the trehalose pair correlation function, at 1.30 *m* for CSFF. The isosurface in red corresponds to regions of high density in the pair correlation function, above 1.24-fold with respect to the bulk. The isosurface in blue represents regions of higher probability density for finding directly H bonded molecules. The central molecule shows a representative conformation of trehalose (nonhydroxyl hydrogens were omitted for clarity). Both isosurfaces were smoothed using a Gaussian filter, as implemented in Chimera. For each lobe, corresponding representative H bonded trehalose pairs are also shown. (c) Conformations corresponding to the left lobe in panel (a). Gray lines represent H-bonds formed between neighboring molecules. (d) Conformations corresponding to the right lobe in panel (a).

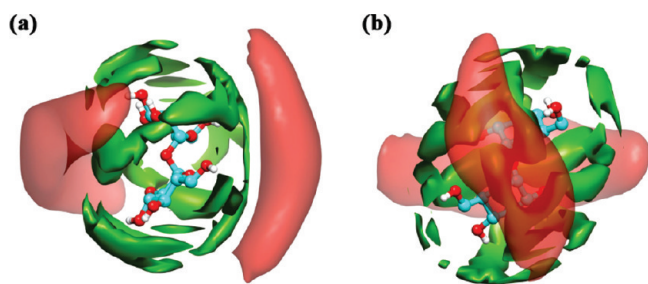


Figure 7. (a, b) Two projections of the spatial density distribution of trehalose–trehalose and trehalose–water pair correlations, at 1.30 *m* for CSFF. The isosurface in red is as in Figure 6a,b. The isosurface in green corresponds to regions of high density in the pair correlation function of trehalose–water (1.11 above the bulk value). The central molecule shows a representative conformation of trehalose, where nonhydroxyl hydrogens were omitted for clarity. Both isosurfaces were smoothed using a Gaussian filter, as implemented in Chimera.

A coordination number of $N_C = 2$ suggests a higher probability of finding sugar molecules bound within or close to the two lobes seen in the pair correlation function (Figure 6a,b). The fact that trehalose shows two preferential binding sites suggests that trehalose clusters can grow approximately linearly, at least when concentrations are not too high. The value of \mathcal{D} for finite clusters at low concentrations, discussed in section 3.4, supports this idea.⁷⁶ At higher concentrations, large branched clusters become more prevalent, while concomitantly the probability of molecules with $N_C > 2$ increases, possibly reflecting the formation of branching junctions. The appearance of molecules with coordination numbers of three and higher, and subsequent branching, could also explain the decrease in the fraction of molecules residing in finite clusters, together with

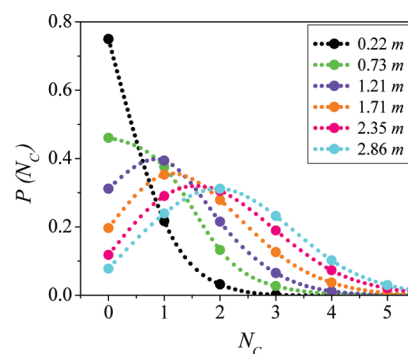


Figure 8. Trehalose molecules tend to form H bonds with an increasing number of neighbors as concentration grows. The probability for a given trehalose coordination number (N_C) at various concentrations. Dotted lines serve as guides to the eye. Results shown are for CSFF; C35 showed similar results.

a corresponding steep increase in X_∞ (Figure 3a). The increase in the number of branching junctions is apparently responsible for the higher probability of percolation.

3.6. The Osmotic Pressure of Aqueous Trehalose Solutions Shows Modest Positive Deviations from Ideal Solution Behavior. Using vapor pressure osmometry (VPO), we measured the osmotic pressure of aqueous trehalose solutions over a wide range of concentrations (0.2–2.4 *m*), at $T = 298 \pm 1$ K. Note, that the highest concentration measured, ~ 2.4 *m*, is in the supersaturated regime.⁷³ For simplicity, the osmotic pressure is discussed in terms of $\tilde{\Pi} = \Pi/RT$ where Π is in units of pressure and $\tilde{\Pi}$ is in osmolal. Figure 9a shows the measured osmotic pressure versus trehalose molal concentration (black circles). The data was fitted with a third order polynomial

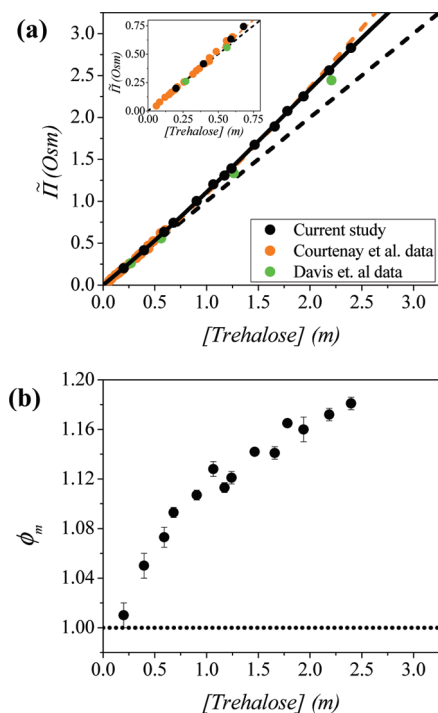


Figure 9. (a) Osmotic pressure of trehalose aqueous solutions versus concentration at $T = 298 \pm 1$ K (black circles). The black solid line represents a third order fit to the data. Experimental standard deviations are smaller than symbol size. Orange circles represent data reproduced (by digitization) from Figure 1 of ref 78, the orange dashed line is a quadratic fit to that data,⁷⁸ and the green circles are reproduced from Figure 2 of ref 79. Inset shows an enlarged region of the low concentration range shown in the main panel. Also shown is the ideal solution behavior (van't Hoff law, black dashed line). (b) Osmotic coefficient ϕ_m derived from data in (a), shown as a function of concentration.

$\tilde{\Pi} = m + am^2 + bm^3$, where m is the concentration in molal. The smallest root-mean-square deviation is found for $a = 0.135$ Osm m^{-2} , $b = -0.026$ Osm m^{-3} (black line). While closely following ideal solution behavior at very low concentrations, at higher concentrations the binary solutions show positive deviations from van't Hoff's law. It is useful to follow these changes with concentration through the osmotic coefficient, $\phi_m = \tilde{\Pi}/m$. Figure 9b shows that, over the concentration range we have tested, $\phi_m > 1$ and that it is concentration dependent. Whereas ϕ_m increases with concentration for the entire range we have tested, the slope of ϕ_m decreased at higher concentrations, possibly even reaching a plateau above a concentration of ~ 2.0 m (Figure 9b).

We have compared our measurements of the osmotic pressure with previously reported data that was collected using similar experimental methodology. Courtenay et al.⁷⁸ measured the osmotic pressure in the range of 0–0.6 m (Figure 9a, orange circles), and fitted their results to a quadratic equation (orange dashed line). These measurements and fit are in excellent agreement with our own measurements in the low concentrations regime, up to about 2.0 m. Davis et al.⁷⁹ measured the osmotic pressure up to concentrations of about 2.2 m. We converted their reported measurements as a function of molarity to a function of molality, using the densities reported by Elias and Elias;⁵³ this data is also close to our data, as presented in Figure 9a (green circles). It seems that small changes in temperature ($T = 297$ – 310 K in ref 78 and $T = 295$ K in ref 79) did not significantly alter this agreement.

Prickett et al.⁸⁰ also reported the osmotic pressure of trehalose solutions, showing negative deviations from ideality below about

1.0 m. However, the method used in that study, based on freezing point depression, better corresponds to the pressure at fairly low temperatures (around freezing). The deviations they found, therefore, probably reflect a dominance of trehalose aggregation over repulsions at those low temperatures, around $T = 273$ K, as further discussed in section 3.8.

While the deviations from an ideal osmotic pressure behavior are quite small, the trehalose deviations from ideality are better evidenced in the corresponding changes in the trehalose molal activity coefficient, γ_T , with concentration (see Supporting Information, Figure S7).

3.7. Comparing Osmotic Pressure Derivatives from Simulation and Experiment. The Kirkwood–Buff (KB) theory of solutions links water–water and water–trehalose pair correlation functions (g_{WW} and g_{WT} , respectively) to the derivative of μ_W , water's chemical potential, with respect to ρ_W , water number density.⁸¹ Therefore, KB theory allows us to make a direct comparison of experiment and simulation through the appropriate derivatives.

Taking the pair correlation functions for every system we simulated, the KB integrals can be calculated using

$$G_{ij} = \int_0^\infty (g_{ij}(r) - 1) 4\pi r^2 dr \quad (3)$$

where i and j are indices of different species in solution (W, water; T, trehalose). Furthermore, the values of G_{WW} and G_{WT} are directly linked to the derivative of the osmotic pressure with water concentration through the following relations:

$$\left(\frac{\partial \mu_W}{\partial \rho_W} \right)_{T,P} = \frac{kT}{\rho_W(1 + \rho_W G_{WW} - \rho_W G_{WT})} \quad (4)$$

$$\left(\frac{\partial \tilde{\Pi}}{\partial \rho_W} \right)_{T,P} = -\frac{m_W}{kT} \left(\frac{\partial \mu_W}{\partial \rho_W} \right)_{T,P} \quad (5)$$

where m_W is the molality of pure water.

The experimental derivative of $\tilde{\Pi}$ with respect to ρ_W can also be calculated for the osmometry data, by using the following relation that converts trehalose molality, m_T , to water number density, ρ_W :

$$\left(\frac{\partial \tilde{\Pi}}{\partial \rho_W} \right)_{T,P} = -\frac{m_W}{\bar{v}_T \rho_W^2} \left(\frac{\partial \tilde{\Pi}}{\partial m_T} \right)_{T,P} \quad (6)$$

where \bar{v}_T is the partial molar volume of trehalose. The value of \bar{v}_T for each sample was interpolated from measurements by Branca et al. at 293 K,⁸² which revealed only small variations in \bar{v}_T over the relevant concentration range. Also, values of ρ_W as a function of molality were interpolated from measurements by Elias and Elias.⁵³

Figure 10a shows $\partial \tilde{\Pi} / \partial \rho_W$ as derived from the simulations and as calculated for the VPO data. For comparison, eq 6 was also used to calculate the derivative for a (hypothetical) ideal solution (black dotted line), where the osmotic pressure derivative with respect to molality is identically 1.0. Both experiment and simulations run with the CSFF force field show behavior that is very close to that expected from a binary solution in which the solvent follows Raoult's law. However, while the experimental derivatives suggest a slight superideal trend, both force fields yield subideal behavior. This discrepancy probably

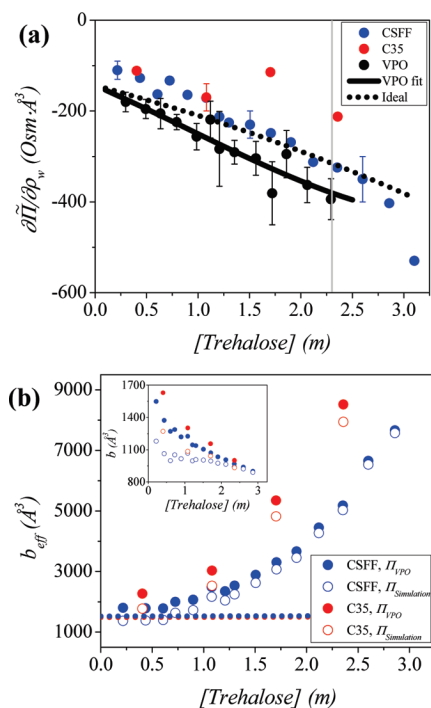


Figure 10. (a) The derivative $\partial\tilde{\Pi}/\partial\rho_w$ versus trehalose molality, shown for simulations and experiments. The vertical gray line represents the experimental solubility limit of trehalose at $T = 298$ K. The derivative was obtained using eqs 4 and 5 for the simulation data and eq 6 for the experimental data. Representative error bars for the simulation data report standard deviations derived using bootstrapping. (b) Effective excluded volume *per particle* (monomers and clusters), b_{eff} , as a function of trehalose molality. The blue and red dotted lines represent the excluded volume of a hard sphere, $4\bar{v}_T$, using \bar{v}_T values calculated from simulations that used CSFF and C35, respectively (see text for details). Inset: Excluded volume *per trehalose molecule*, b , as a function of trehalose molality. Color scheme for both force fields is as in Figure 3b.

reflects an overaggregative nature of the simulated trehalose molecules.⁸³ The C35 force field shows an even more pronounced divergence from ideality, as expected from the higher tendency of its trehalose molecules to self-associate.

3.8. A Simple Model Links Trehalose Clustering with Osmotic Pressure. The near ideal behavior of aqueous trehalose solutions, seen in both simulation and experiment, suggests a fine balance between intermolecular attractions and repulsions. We propose a simple model that accounts for the strong trehalose–trehalose attractive interactions by explicitly considering trehalose clustering, while also considering steric excluded volume trehalose–trehalose interactions that are effectively repulsive. The balance of these two forces is sufficient to explain why experimental ϕ_m is larger than 1.0 but does not rise even further with concentration, as seen in Figure 9b. Further, this simple equation of state can explain how $\partial\tilde{\Pi}/\partial\rho_w$ for the CSFF simulation remains very close to ideal, even though trehalose self-association dramatically reduces the effective concentration of particles (monomers or clusters), as witnessed in Figure 3b.

First, we make the simplifying assumption that attractions leading to trehalose clustering could be expressed solely by the reduction in the effective number of solvated particles (expressed as the sum of trehalose clusters and monomers) in solution, N_{eff} . Another simplifying assumption is to effectively include repulsions through the reduction in free volume due to trehalose–trehalose hard core interactions. We then propose the following simple equation of state:

$$\tilde{\Pi} = \frac{N_{\text{eff}}}{N_{\text{AV}}(V - N_{\text{eff}}b_{\text{eff}})} = \frac{C_{\text{eff}}}{1 - N_{\text{AV}}C_{\text{eff}}b_{\text{eff}}} \quad (7)$$

where V is the system volume, b_{eff} is the effective excluded volume *per particle*, $C_{\text{eff}} = \langle N_{\text{eff}} \rangle / N_{\text{AV}}V$ is the effective molar concentration of solvated particles.

Equation 7 can now be used to derive b_{eff} at each concentration, as long as the number of aggregates and osmotic pressure are known. The values of $\tilde{\Pi}$ are available from experiments on the one hand, and on the other hand they can be derived for simulations by integrating over $\partial\tilde{\Pi}/\partial\rho_w$, Figure 10a, and by assuming ideal behavior at concentrations lower than 0.22 m (the lowest simulated concentration). For both experiments and simulations, we use estimates for the numbers of trehalose clusters from the simulations.

Figure 10b shows the dependence of b_{eff} on trehalose molality, calculated using fits to the measured (full circles) and calculated (empty circles) $\tilde{\Pi}$ versus molality, Figure 10a. Both force fields yield very similar estimates of b_{eff} , as derived based on both experimental and simulation $\tilde{\Pi}$ data sets. Clearly, as concentration increases, clusters become larger and therefore b_{eff} increases. The inset of Figure 10b shows the mean excluded volume *per molecule*, $b = b_{\text{eff}}C_{\text{eff}}/C$. As concentration increases, b decreases, reflecting trehalose self-association that reduces the excluded volume on a *per molecule* basis.

The extrapolation of b_{eff} and b to infinite dilution gives the excluded volume for isolated molecules, b_0 . The values of b_0 were compared with the partial molar volume of trehalose at infinite dilution, \bar{v}_T^0 , using the expression $4\bar{v}_T^0f$, where f is a constant that depends on molecular shape. For a perfect sphere $f = 1$, but for any other shape $f > 1$.⁸⁴

The values of $\bar{v}_T(m)$ derived from simulation deviated from available experimental data by about 7%–10% over the entire concentration range (See Supporting Information, Figure S8). Specifically, the values for \bar{v}_T^0 from simulations were 230 mL/mol and 224 mL/mol for CSFF and C35, respectively, evaluated as described in the Supporting Information, while the corresponding extrapolation of the experimental data gives 208 mL/mol⁵³ and 209 mL/mol.⁸² The higher $\bar{v}_T(m)$ in simulations may help compensate for the overaggregative nature of the force fields, eventually yielding an equation of state that is close to the experimental. These compensating interactions, in turn, may explain the near ideal behavior of $\partial\tilde{\Pi}/\partial\rho_w$ by CSFF. Both plots of b_{eff} and b (Figure 10b) for C35 and CSFF using the experimentally determined $\tilde{\Pi}$ gave $f > 1$, as expected from the nonspherical molecular shape of trehalose. For comparison, the expected excluded volume of a perfect hard sphere, $4\bar{v}_T(m)$, is also shown in Figure 10b (blue and red dotted lines). Interestingly, at lower temperatures, where attractions should be more dominant than repulsions, experiments indeed find that the osmotic pressure shows subideal behavior at low concentrations,⁸⁰ as mentioned in section 3.6.

4. Concluding Remarks

We have studied the self-association of trehalose molecules in binary aqueous solutions over a wide range of concentrations. Simulations show that trehalose molecules aggregate into clusters that increase in size with increasing concentration (Figures 2, 3). At the percolation threshold, estimated in simulations to lie between 1.5 and 2.2 m , infinite clusters form, and the concentration of finite clusters drops (Figures 3, 4). While intermolecular H bonds dominate these trehalose–trehalose attractions (Figure 6), excluded volume effects are responsible

for effective mutual repulsions between molecules. The delicate balance between these forces causes the osmotic pressure in simulations of trehalose aqueous solutions to be relatively close to an ideal van't Hoff behavior, with a small negative deviation from ideality (Figure 10). Whereas experimental VPO measurements suggest a clear positive deviation from ideality, the near saturation of the osmotic coefficient at ~ 2.0 *m* testifies to the balance between both attractive and repulsive contributions (Figures 9, 10).

The high propensity for self-association by trehalose, simulated using both CSFF and C35, is quite ubiquitous and seen also for other force fields and simulated molecules.⁸³ Whereas the simulations were conducted at concentrations greater than those at which the force fields were calibrated, the simulated self-association should not be regarded as a mere artifact of the force field parametrization alone. In fact, this is an intrinsic tendency of trehalose molecules, that is not shared by all alcohols and polyols; ethanol, for example, almost does not form clusters.⁴¹ This tendency is, however, shared to some extent with sucrose, which is also known to form clusters in solution^{29,33–35,41} and has a stronger tendency for solute–solute attractive interactions compared to other osmolytes.⁸⁵

Beyond comparisons to the dynamic properties of similar trehalose solutions,⁶⁹ our study emphasizes the need to compare thermodynamic solution properties found experimentally, such as solution osmotic pressures, to those in simulation, as a means of validating and potentially improving empirical force fields.⁸⁶ These solution equilibrium properties are determined by the balance between intermolecular attractions and excluded volume effects. We conclude that, although over a wide concentration range both the CSFF and C35 force fields yield results that compare favorably with experimentally derived osmotic pressures, both also share a slight overaggregative propensity that is canceled to some extent by steric interactions.

Multiple experimental indicators underscore trehalose self-association and the important subsequent implication to solution structure and properties. For highly concentrated solutions, this aggregative tendency is manifested in trehalose's high glass transition temperature.²⁶ At lower (though still high) concentrations, trehalose cluster's percolation can be related to significant changes in dynamic properties.^{30,32,34,37} For example, it has been speculated that an aggregative process might be reflected in the dependence of trehalose diffusion coefficient on concentration.^{39,40} Further testimony to trehalose clustering is the appearance of fine small particles of trehalose in freeze-fractured trehalose aqueous solutions,⁸⁷ though these are much larger (20–30 nm) than the particles we observe in simulations. Trehalose self-association properties are important because they could possibly be linked to trehalose mechanisms of biopreservation and particularly to its protein stabilizing effect. It would be interesting to further study how cluster formation and trehalose percolation may influence protein stability and, in particular, how this unique carbohydrate might modulate protein conformational free energy landscape.

Acknowledgment. We thank R. Granek and A. D. MacKerell, Jr. for helpful discussions and U. Raviv for use of the osmometer. We also thank R. Politi for help with analysis scripts. The financial support from the Israel Science Foundation (ISF Grant No. 1011/07) as well as the allocation for a high-performance computer cluster facility (ISF Grant No. 1012/07) are gratefully acknowledged. The Fritz Haber Research Center is supported by the Minerva Foundation, Munich, Germany.

Supporting Information Available: Thermodynamic properties as a function of trehalose concentration: Density (Figure S1) and partial molar volume (Figure S8). Hydrogen–hydrogen pair correlation function (Figure S2), and probability distribution for hydrogen bonds (Figure S3) in pure water and in trehalose solution. Structural order parameter in trehalose solution (Figure S4). Spatial density distribution of trehalose pair correlation (Figures S5 and S6). Trehalose molal activity coefficient (Figure S7). This material is available free of charge via the Internet at <http://pubs.acs.org>.

References and Notes

- (1) Anchordoguy, T. J.; Rudolph, A. S.; Carpenter, J. F.; Crowe, J. H. *Cryobiology* **1987**, *24*, 324.
- (2) Green, J. L.; Angell, C. A. *J. Phys. Chem.* **1989**, *93*, 2880.
- (3) Rudolph, A. S.; Crowe, J. H. *Cryobiology* **1985**, *22*, 367.
- (4) Crowe, J. H.; Carpenter, J. F.; Crowe, L. M. *Annu. Rev. Physiol.* **1998**, *60*, 73.
- (5) Crowe, J. H.; Crowe, L. M.; Oliver, A. E.; Tsvetkova, N.; Wolkers, W.; Tablin, F. *Cryobiology* **2001**, *43*, 89.
- (6) Crowe, L. M. *Comp. Biochem. Physiol., Part A: Mol. Integr. Physiol.* **2002**, *131*, 505.
- (7) Crowe, J. H.; Hoekstra, F. A.; Crowe, L. M. *Annu. Rev. Physiol.* **1992**, *54*, 579.
- (8) Politi, R.; Harries, D. *Chem. Commun.* **2010**, *46*, 6449.
- (9) Harries, D.; Rosgen, J. A practical guide on how osmolytes modulate macromolecular properties. *Biophysical Tools for Biologists: Vol. 1 In Vitro Techniques*; Elsevier Academic Press Inc: San Diego, 2008; Vol. 84; p 679.
- (10) Kaushik, J. K.; Bhat, R. J. *Biol. Chem.* **2003**, *278*, 26458.
- (11) Xie, G. F.; Timasheff, S. N. *Biophys. Chem.* **1997**, *64*, 25.
- (12) Patist, A.; Zoerb, H. *Colloids Surf., B* **2005**, *40*, 107.
- (13) Kanas, T.; Acker, J. P. *Cell Preserv. Technol.* **2006**, *4*, 253.
- (14) Jain, N. K.; Roy, I. *Protein Sci.* **2009**, *18*, 24.
- (15) Almeida, A. M.; Cardoso, L. A.; Santos, D. M.; Torne, J. M.; Fevereiro, P. S. *In Vitro Cell. Dev. Biol.: Plant* **2007**, *43*, 167.
- (16) Guo, N.; Puhlev, I.; Brown, D. R.; Mansbridge, J.; Levine, F. *Nat. Biotechnol.* **2000**, *18*, 168.
- (17) Magazu, S.; Migliardo, F.; Affouard, F.; Descamps, M.; Telling, M. T. F. *J. Chem. Phys.* **2010**, *132*, 184512.
- (18) Gharsallaoui, A.; Roge, B.; Mathlouthi, M. *Food Chem.* **2008**, *106*, 1329.
- (19) Cesaro, A.; De Giacomo, O.; Sussich, F. *Food Chem.* **2008**, *106*, 1318.
- (20) Carpenter, J. F.; Crowe, J. H. *Biochemistry* **1989**, *28*, 3916.
- (21) Belton, P. S.; Gil, A. M. *Biopolymers* **1994**, *34*, 957.
- (22) Branca, C.; Magazu, S.; Maisano, G.; Migliardo, P. *J. Chem. Phys.* **1999**, *111*, 281.
- (23) Cordone, L.; Cottone, G.; Giuffrida, S. J. *Phys.: Condens. Matter* **2007**, *19*, 205110.
- (24) Lerbret, A.; Affouard, F.; Bordat, P.; Hedoux, A.; Guinet, Y.; Descamps, M. *J. Chem. Phys.* **2009**, *131*, 245103.
- (25) Lins, R. D.; Pereira, C. S.; Hunenberger, P. H. *Proteins: Struct., Funct., Bioinf.* **2004**, *55*, 177.
- (26) Perić-Hassler, L.; Hansen, H. S.; Baron, R.; Hunenberger, P. H. *Carbohydr. Res.* **2010**, *345*, 1781.
- (27) Sidebottom, D. L.; Tran, T. D. *Phys. Rev. E* **2010**, *82*, 051904.
- (28) Sonoda, M. T.; Skaf, M. S. J. *Phys. Chem. B* **2007**, *111*, 11948.
- (29) Molinero, V.; Cagin, T.; Goddard, W. A. *Chem. Phys. Lett.* **2003**, *377*, 469.
- (30) Rampp, M.; Buttersack, C.; Ludemann, H. D. *Carbohydr. Res.* **2000**, *328*, 561.
- (31) Champion, D.; Hervet, H.; Blond, G.; LeMeste, M.; Simatos, D. J. *Phys. Chem. B* **1997**, *101*, 10674.
- (32) Ekdawi-Sever, N.; de Pablo, J. J.; Feick, E.; von Meerwall, E. J. *Phys. Chem. A* **2003**, *107*, 936.
- (33) Lerbret, A.; Bordat, P.; Affouard, F.; Hedoux, A.; Guinet, Y.; Descamps, M. *J. Phys. Chem. B* **2007**, *111*, 9410.
- (34) Lerbret, A.; Bordat, P.; Affouard, F.; Descamps, M.; Migliardo, F. J. *Phys. Chem. B* **2005**, *109*, 11046.
- (35) Lerbret, A.; Affouard, F.; Bordat, P.; Hedoux, A.; Guinet, Y.; Descamps, M. *Chem. Phys.* **2008**, *345*, 267.
- (36) Bordat, P.; Lerbret, A.; Demaret, J. P.; Affouard, F.; Descamps, M. *Europhys. Lett.* **2004**, *65*, 41.
- (37) Conrad, P. B.; de Pablo, J. J. *J. Phys. Chem. A* **1999**, *103*, 4049.
- (38) Branca, C.; Magazu, S.; Maisano, G.; Telling, M. T. F. *J. Phys. Chem. B* **2004**, *108*, 17069.
- (39) Magazu, S.; Maisano, G.; Migliardo, P.; Villari, V. J. *Chem. Phys.* **1999**, *111*, 9086.

- (40) Magazu, S.; Maisano, G.; Middendorf, H. D.; Migliardo, P.; Musolino, A. M.; Villari, V. *J. Phys. Chem. B* **1998**, *102*, 2060.
- (41) Liu, F. F.; Ji, L.; Zhang, L.; Dong, X. Y.; Sun, Y. *J. Chem. Phys.* **2010**, *132*, 225103.
- (42) Pereira, C. S.; Hunenberger, P. H. *Mol. Simul.* **2008**, *34*, 403.
- (43) Pereira, C. S.; Hunenberger, P. H. *Biophys. J.* **2008**, *95*, 3525.
- (44) Sum, A. K.; Faller, R.; de Pablo, J. J. *Biophys. J.* **2003**, *85*, 2830.
- (45) Phillips, J. C.; Braun, R.; Wang, W.; Gumbart, J.; Tajkhorshid, E.; Villa, E.; Chipot, C.; Skeel, R. D.; Kale, L.; Schulten, K. *J. Comput. Chem.* **2005**, *26*, 1781.
- (46) Ha, S. N.; Giammona, A.; Field, M.; Brady, J. W. *Carbohydr. Res.* **1988**, *180*, 207.
- (47) Palma, R.; Zuccato, P.; Himmel, M. E.; Liang, G.; Brady, J. W. Molecular Mechanics Studies of Cellulases. In *Glycosyl Hydrolases for Biomass Conversion*; Himmel, M. E., Baker, J. O., Saddler, J. N., Eds., American Chemical Society: Washington, DC, 2000; pp 112.
- (48) Kuttel, M.; Brady, J. W.; Naidoo, K. J. *J. Comput. Chem.* **2002**, *23*, 1236.
- (49) Guvench, O.; Greene, S. N.; Kamath, G.; Brady, J. W.; Venable, R. M.; Pastor, R. W.; MacKerell, A. D. *J. Comput. Chem.* **2008**, *29*, 2543.
- (50) Guvench, O.; Hatcher, E.; Venable, R. M.; Pastor, R. W.; MacKerell, A. D. *J. Chem. Theory Comput.* **2009**, *5*, 2353.
- (51) Humphrey, W.; Dalke, A.; Schulten, K. *J. Mol. Graphics* **1996**, *14*, 33.
- (52) Pettersen, E. F.; Goddard, T. D.; Huang, C. C.; Couch, G. S.; Greenblatt, D. M.; Meng, E. C.; Ferrin, T. E. *J. Comput. Chem.* **2004**, *25*, 1605.
- (53) Elias, M. E.; Elias, A. M. *J. Mol. Liq.* **1999**, *83*, 303.
- (54) Branca, C.; Magazu, S.; Maisano, G.; Migliardo, F.; Migliardo, P.; Romeo, G. *J. Phys. Chem. B* **2001**, *105*, 10140.
- (55) Cesaro, A.; Magazu, V.; Migliardo, F.; Sussich, F.; Vadalà, M. *Physica B* **2004**, *350*, E367.
- (56) Kumar, R.; Schmidt, J. R.; Skinner, J. L. *J. Chem. Phys.* **2007**, *126*.
- (57) Luzar, A.; Chandler, D. *Phys. Rev. Lett.* **1996**, *76*, 928.
- (58) Politi, R.; Sapir, L.; Harries, D. *J. Phys. Chem. A* **2009**, *113*, 7548.
- (59) Guo, F.; Friedman, J. M. *J. Phys. Chem. B* **2009**, *113*, 16632.
- (60) Hedoux, A.; Willart, J. F.; Ionov, R.; Affouard, F.; Guinet, Y.; Paccou, L.; Lerbret, A.; Descamps, M. *J. Phys. Chem. B* **2006**, *110*, 22886.
- (61) Hedoux, A.; Willart, J. F.; Paccou, L.; Guinet, Y.; Affouard, F.; Lerbret, A.; Descamps, M. *J. Phys. Chem. B* **2009**, *113*, 6119.
- (62) Kuffel, A.; Zielkiewicz, J. *J. Chem. Phys.* **2010**, *133*, 035102.
- (63) Espinosa, E.; Molins, E.; Lecomte, C. *Chem. Phys. Lett.* **1998**, *285*, 170.
- (64) Lerbret, A.; Bordat, P.; Affouard, F.; Guinet, Y.; Hedoux, A.; Paccou, L.; Prevost, D.; Descamps, M. *Carbohydr. Res.* **2005**, *340*, 881.
- (65) Branca, C.; Magazu, S.; Maisano, G.; Migliardo, P. *J. Phys. Chem. B* **1999**, *103*, 1347.
- (66) Lee, S. L.; DeBenedetti, P. G.; Errington, J. R. *J. Chem. Phys.* **2005**, *122*, 204511.
- (67) Errington, J. R.; DeBenedetti, P. G. *Nature* **2001**, *409*, 318.
- (68) Galema, S. A.; Hoiland, H. J. *J. Phys. Chem.* **1991**, *95*, 5321.
- (69) Venable, R. M.; Hatcher, E.; Guvench, O.; MacKerell, A. D.; Pastor, R. W. *J. Phys. Chem. B* **2010**, *114*, 12501.
- (70) Bunde, A.; Havlin, S. *Fractals and disordered systems*, 2nd rev. and enlarged ed.; Springer: Berlin, New York, 1996.
- (71) Dewey, T. G. *Fractals in molecular biophysics*; Oxford University Press: Oxford, New York, 1997.
- (72) Sahimi, M. *Applications of percolation theory*; Taylor & Francis: London, Bristol, PA, 1994.
- (73) Miller, D. P.; dePablo, J. J.; Corti, H. *Pharm. Res.* **1997**, *14*, 578.
- (74) Zilman, A. G.; Safran, S. A. *Phys. Rev. E* **2002**, *66*, 051107.
- (75) Coniglio, A.; Stanley, H. E.; Klein, W. *Phys. Rev. Lett.* **1979**, *42*, 518.
- (76) Rubinstein, M.; Colby, R. H. *Polymer physics*; Oxford University Press: Oxford, New York, 2003.
- (77) Liu, Q.; Schmidt, R. K.; Teo, B.; Karplus, P. A.; Brady, J. W. *J. Am. Chem. Soc.* **1997**, *119*, 7851.
- (78) Courtenay, E. S.; Capp, M. W.; Anderson, C. F.; Record, M. T. *Biochemistry* **2000**, *39*, 4455.
- (79) Davis, D. J.; Burlak, C.; Money, N. P. *Mycol. Res.* **2000**, *104*, 800.
- (80) Prickett, R. C.; Elliott, J. A. W.; McGann, L. E. *Cryobiology* **2010**, *60*, 30.
- (81) Kirkwood, J. G.; Buff, F. P. *J. Chem. Phys.* **1951**, *19*, 774.
- (82) Branca, C.; Magazu, S.; Maisano, G.; Migliardo, P. *J. Biol. Phys.* **2000**, *26*, 295.
- (83) Weerasinghe, S.; Bae Gee, M.; Kang, M.; Benteitis, N.; Smith, P. E. Developing Force Fields From the Microscopic Structure of Solutions: The Kirkwood-Buff Approach. In *Modeling solvent environments: applications to simulations of biomolecules*; Feig, M., Ed.; Wiley-VCH: Weinheim, 2010; p 55.
- (84) Isihara, A. *J. Chem. Phys.* **1950**, *18*, 1446.
- (85) Rosgen, J.; Pettitt, B. M.; Bolen, D. W. *Biochemistry* **2004**, *43*, 14472.
- (86) Ploetz, E. A.; Benteitis, N.; Smith, P. E. *Fluid Phase Equilib.* **2010**, *290*, 43.
- (87) Uchida, T.; Nagayama, M.; Shibayama, T.; Gohara, K. *J. Cryst. Growth* **2007**, *299*, 125.

JP109780N